Structural phase transition and magnetism in hexagonal $SrMnO_3$ by magnetization measurements and by electron, x-ray, and neutron diffraction studies

A. Daoud-Aladine,[1] C. Martin,[2,1] L. C. Chapon,[1] M. Hervieu,[2] K. S. Knight,[1] M. Brunelli,[3] and P. G. Radaelli[1,4]
[1]*ISIS facility, Rutherford Appleton Laboratory-CCLRC, Chilton, Didcot, Oxfordshire, OX11 0QX, United Kingdom*
[2]*Laboratoire CRISMAT-UMR, 6508 ENSI CAEN, 6, Marechal Juin, 14050 Caen, France*
[3]*European Synchrotron Radiation Facility, BP220, F-38043 Grenoble Cedex, France*
[4]*Department of Physics and Astronomy, University College London, Gower Street, London WC1E 6BT, United Kingdom*
(Received 5 September 2006; revised manuscript received 21 December 2006; published 21 March 2007)

The structural and magnetic properties of the hexagonal four-layer form of $SrMnO_3$ have been investigated by combining magnetization measurements, electron diffraction, and high-resolution synchrotron x-ray and neutron powder diffraction. Below 350 K, there is subtle structural phase transition from hexagonal symmetry (space group $P6_3/mmc$) to orthorhombic symmetry (space group $C222_1$) where the hexagonal metric is preserved. The second-order phase transition involves a slight tilting of the corner-sharing Mn_2O_9 units composed of two face-sharing MnO_6 octahedra and the associated displacement of Sr^{2+} cations. The phase transition is described in terms of symmetry-adapted displacement modes of the high symmetry phase. Upon further cooling, long range magnetic order with propagation vector $\mathbf{k}=(0,0,0)$ sets in below 300 K. The antiferromagnetic structure, analyzed using representation theory, shows a considerably reduced magnetic moment indicating the crucial role played by direct exchange between Mn centers of the Mn_2O_9 units.

DOI: 10.1103/PhysRevB.75.104417 PACS number(s): 75.47.Lx, 61.14.−x, 61.10.−i, 61.12.−q

I. INTRODUCTION

Transition metal oxides show remarkable physical properties, such as colossal magnetoresistance in manganites[1] or superconductivity in cuprates,[2] which after decades of research, remain still partly understood. This reflects our understanding of the structural, electronic and magnetic phenomena, which is well established only in the limit where the systems show localized or itinerant electron behavior.[3] Doping with electrons or holes is the canonical method to explore the intermediate regime. For example, in $R_{1-x}D_xMnO_3$ manganese perovskites (R: trivalent cation, D: divalent cation), the Mn valence is formally intermediate $3+x$, affecting the electrical conductivity and leading to a complex phase diagram.

However, even undoped compounds display an intriguing evolution of their magnetic properties as the geometry and coordination are changed. For example, in the $RMnO_3$ and $DMnO_3$ end members of the $R_{1-x}D_xMnO_3$ series, Mn has undoubtedly well localized electrons, making these compounds prototype antiferromagnetic (AF) Mott insulators. Their magnetic properties fit a Heisenberg picture, in which superexchange (SE) interactions couple high spin $Mn^{3+}(S=2)$ and $Mn^{4+}(S=3/2)$ ions at $x=0$ and $x=1$, respectively.[4–6] By contrast, the magnetic properties of some hexagonal manganese halides containing single valent Mn ions are unusual. $CsMnBr_3$ (Ref. 7) and $CsMnI_3$ (Ref. 8) compounds containing $S=5/2$ high spin Mn^{2+} ions arranged in infinite strings of face-sharing MnO_6 octahedra parallel to the c axis, from which frustration between direct and superexchange interactions, of different signs, is expected. Exchange frustration in the basal plane also brings about chirality of the magnetic state and a spin dynamic corresponding to new universality classes.[7] One may be tempted to conclude that these unusual magnetic properties arise from the quasi-one-dimensional nature of the exchange, combined with easy axis anisotropy. However, isostructural $BaMnO_3$ ($S=3/2$) does not show such effects, but it has instead a simple antiferromagnetic structure and rather classical magnetic behavior with a value of the ordered moment saturating at low temperatures.[9]

In order to separate the influence upon the magnetic properties of the lattice geometry from more conventional chemical effects, the study of polymorphic compounds, which display different stable or metastable structures with the same chemical composition is particularly valuable. As discussed by Nagas and Roth,[10] the stability of the structures adopted by ABX_3 compounds depends on the tolerance factor $t=(r_A+r_X)/\sqrt{2}(r_B+r_X)$, where r_A is the average ionic radius of the A-site cations, while r_B and r_X are those of the B-site metal and of the anion (oxygen, halogen, or chalcogen). Most manganites have $t\leqslant 1$, and crystallize in orthorhombic or rhombohedral perovskite structures showing cooperative tilting of the corner-sharing MnO_6 array with respect to the ideal cubic perovskite. For sufficiently large r_A ($t>1$), materials adopt a different hexagonal symmetry, as in the case of $BaMnO_3$ and the aforementioned halides. For $t\gtrsim 1$, polytypes are obtained depending on the synthesis procedure.[10,11] These polytypes are characterized by the stacking sequence of the AO_3 layers, which controls how the MnO_6 octahedra arrange. Octahedra are sharing corners across the central AO_3 layer of $\cdots abc\cdots$ sequences, while they share faces across $\cdots aba\cdots$ type sequences.

For example, synthesized at ambient pressure in air, $SrMnO_3$ ($t=1.05$) has a four layer ($4L$) $abac$ stacking sequence of SrO_3 layers as shown in Fig. 1, whereas modified synthesis routines are required to obtain the cubic perovskite.[12] $4L$ is a rather rare polytype among ABX_3 compounds, and represents an intermediate case between the hexagonal ($2L$) polytype adopted by $BaMnO_3$, and the famil-

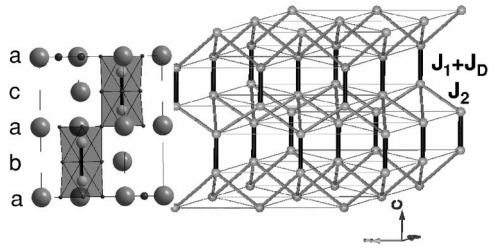

FIG. 1. Left panel: Crystal structure of $SrMnO_3$ viewed along the [110] direction. The Sr, Mn, and O atoms are shown as large grey spheres, small grey spheres, and black spheres, respectively. Face-sharing MnO_6 octahedra are also represented as transparent grey units; right panel: magnetic exchange topology of the Mn sublattice. Black bonds represent magnetic exchange between Mn ions of the Mn_2O_9 units, composed of antiferromagnetic direct exchange (J_D) and ferromagnetic superexchange (J_1). Grey bonds represent superexchange interactions (J_2) between Mn ions of the hexagonal units. See text for details.

iar perovskite structure of $CaMnO_3$ containing only corner sharing octahedra. It is therefore interesting to study the magnetism in $SrMnO_3$ in comparison with that of the perovskite and $2L$ hexagonal materials. This could also help to shed light on the striking differences of magnetic behavior in isostructural $CsMnBr_3$ and $BaMnO_3$. In $SrMnO_3$, a complex magnetic behavior is expected from the exchange topology, which results from the arrangement of pairs of face-sharing MnO_6 octahedra linked by their corners. In this structure, direct Mn-Mn exchange interactions between Mn^{4+} ions in face-sharing octahedra (J_D) compete with the 90° AF-SE linkages through the face shared by MnO_6 octahedra (J_1) as in $BaMnO_3$, and 180° AF-SE linkages across the common oxygen of corner-sharing MnO_6 octahedra (J_2), as in $CaMnO_3$. As in several hexagonal transition metal oxides or sulfides, J_D is probably very strong, since the metal-metal distance is much smaller than that observed in the corresponding intermetallic compounds containing the same transition metal element.[13,14]

As first noticed by Battle *et al.*,[15] $SrMnO_3$ shows unusual magnetic properties: the magnetization data, which we have also measured (see Fig. 2) shows a transition above room temperature ($T_s \sim 350$ K), but neutron powder diffraction (NPD) demonstrates that this does not correspond to the AF ordering. AF order sets in only at lower temperatures, where zero field cooled and field cooled $M(T)$ curves deviate ($T_N = 278$ K).[15] Recently, Raman spectroscopy was used to evidence a structural transformation in $SrMnO_3$ below 200 K.[16] To explain the subtle difference observed by Raman spectroscopy, the authors proposed a $4L$ to $6L$ transition, allowing the hexagonal symmetry to be retained. In this article, we present a detailed study of the magnetic and structural properties of $SrMnO_3$, using in combination electron microscopy, neutron powder diffraction (NPD), and high-resolution synchtrotron x-ray powder diffraction (HR-SXPD).

II. EXPERIMENTAL

Polycrystalline samples of $SrMnO_3$ were synthesized by solid-state reaction in air of a stoichiometric mixture (1:0.5)

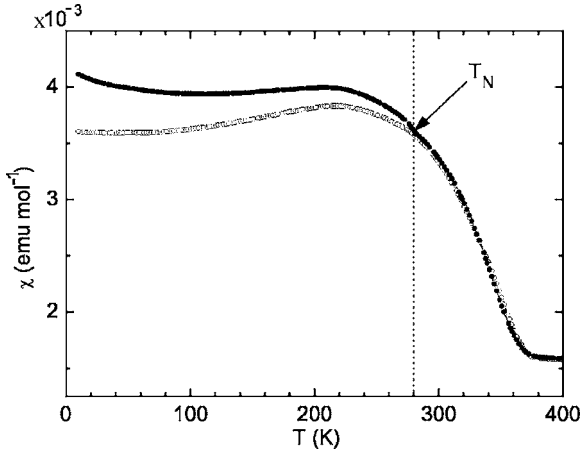

FIG. 2. dc magnetic susceptibility of $SrMnO_3$ under a magnetic field of 1000 Oe. Data in zero-field cooled (grey symbols) and field cooled (black) conditions are shown.

of $SrCO_3$ and Mn_2O_3. The powder was heated at 950 °C during two weeks with intermediate grindings, then pelletized and sintered at 1000 °C for 12 h. This low-temperature synthesis was determined from the phase diagrams[10,11] as the best route to obtain pure hexagonal $4L$ structure without oxygen deficiency. Samples quality and stoichiometry were determined by preliminary neutron diffraction measurements.

At room temperature, the reconstruction of the reciprocal space was carried out with a JEOL 200 CX electron microscope and high resolution electron microscopy (HREM) images at room temperature were recorded using a TOPCON 002B microscope (Cs=0.4 mm). The electron diffraction patterns versus temperature were collected with a JEOL 2010 electron microscope operating at 200 kV and equipped with a double-tilt liquid N_2 sample holder (tilt ±30°, ±45°, and 90 K$<T<$300 K). All the patterns were recorded under the same experimental conditions, i.e., the same exposure time, the same electron beam alignment and the same beam intensity and increasing the temperature from 90 to 300 K, in steps of 10 degrees, waiting for temperature stabilization before recording. The three microscopes are equipped with energy dispersive analysis spectrometers (EDS), which allows determination of the Sr/Mn ratio.

Magnetic susceptibility was collected under a magnetic field of 1000 Oe under zero-field cooled (ZFC) and field cooled (FC) processes. Data were collected on warming between 2 and 400 K at a sweep rate of 1 K/min, using a vibrating sample magnetometer (Quantum Design, PPMS).

High resolution synchrotron and time-of-flight neutron powder diffraction data were collected at 100 and 350 K, using the ID31 beam line at the ESRF, Grenoble with a wavelength $\lambda = 0.30001(2)$ Å, and HRPD at the ISIS Facility (U.K.), respectively. Subsequent medium-resolution neutron diffraction data were collected on the GEneral Materials (GEM) Diffractometer of the ISIS facility to study the temperature dependence of the crystal structure and the magnetic structure. Data sets at temperature between 1.9 and 300 K with 25 K steps were collected on warming using a standard He cryostat. The diffraction patterns were used to refine the $SrMnO_3$ structure by the Rietveld method[17] using the

FULLPROF suite (Ref. 18). Symmetry analysis for the structural and magnetic phase transitions was performed using the BASIREPS program, part of the FULLPROF suite as well as programs available on the Bilbao Crystallographic Server.[19]

III. RESULTS

A. Magnetization measurements

The dc magnetic susceptibility of $SrMnO_3$ between 2 and 400 K is reported in Fig. 2. Plot of the inverse susceptibility, not shown, indicates that a Curie-Weiss behavior is not obeyed in this temperature range, in agreement with earlier results.[20] However, our results below 400 K are qualitatively different than that previously reported. Below 380 K, there is a clear upturn in the susceptibility followed by a relatively shallow decrease below 300 K. The upturn could be associated with the structural phase transition reported herein, and discussed in the following sections, as evidenced by x-ray and neutron diffraction. However, it was impossible to track precisely the structural details as a function of temperature due to the extremely weak intensities of the superlattice reflections and therefore confirm unambiguously the correlation between structural and magnetic behaviors. Also, this upturn could be associated to short-range magnetic correlations within the face-sharing MnO_6 octahedra, as suggested by Battle *et al.*[15]

At lower temperatures ($T<300$ K) where χ decreases, the behavior is clearly reminiscent of antiferromagnets. This is in agreement with previous work, in particular with the large negative Weiss temperature of −1210 K derived from susceptibility measurements at high temperature.[20] The determination of the Néel temperature from susceptibility alone is not straightforward due to the broad maximum observed in the variation of χ. Battle and co-workers identified a Néel temperature of 278 K from Mössbauer spectroscopy on Fe-doped samples.[15] Our measurements suggest the same Néel transition temperature since the susceptibility curves in field cooled (FC) and zero-field cooled (ZFC) conditions deviates at around 280 K. Moreover, that coincides with the onset of a long-range ordered antiferromagnetic structure determined from our neutron diffraction experiment, as discussed below.

B. Crystal structure

In this section, we report a detailed crystallographic characterization of $SrMnO_3$ from electron microscopy and high-resolution x-ray and neutron powder diffraction experiments.

1. Transmission electron microscopy

The sample homogeneity have been checked by the EDS and electron diffraction analysis of a large number of crystallites, which all have an Sr/Mn ratio=1 in the limit of the accuracy of the technique. The reconstruction of the reciprocal space was carried out by tilting the sample around the crystallographic axes. It gives a hexagonal cell with $a \approx 5.45$ Å $\approx \sqrt{2}a_p$ (a_p is the parameter of the ideal cubic perovskite cell), $c \approx 9.06$ Å and the extinction condition $hh2\bar{h}=2n$. These results are consistent with the 4 L polytype proposed for $SrMnO_3$ as well as the space group $P6_3/mmc$ previously reported.[10,11] The $[1\bar{1}0]$ ED pattern at room temperature is given in Fig. 3(a) The quality of the crystallites was checked using HREM, in order to detect the presence of any intergrowth defects (variations in the layer stacking along $\vec{c}$, i.e., the presence of different polytypes). The lattice images, not shown, confirm that the stacking of the 4L structure is quite perfect. The density of defects is very low (of the order a few events for a nanometer-sized crystallite), which is rather rare in the hexagonal polytypes, allowing one to conclude that these defect do not significantly affect the symmetry.

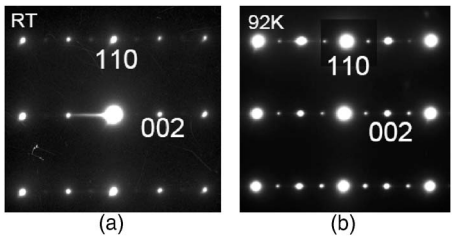

FIG. 3. $[1\bar{1}0]$ ED pattern of $SrMnO_3$ at RT (a) and 92 K (b). The low temperature data shows the appearance of another set of weak reflections $hh2\bar{h}l$ l=no condition which clearly violate the mirror c. A careful rotation around $\vec{c}^*$, selecting the $[hk0]$ ED patterns with large h and k values, shows that, in our conditions of reflection, the conditions $00l$: $l=2n+1$ are scarcely visible but not null and hence, are not due to double diffraction.

The reciprocal space was also measured at 90 K, tilting especially around the $\vec{c}^*$ axis. One clearly observes two important points: first, the lattice parameters remain unchanged, especially c^*, attesting that the 4L stacking mode is retained and second, the appearance of another set of weak reflections $hh2\bar{h}l$ l=no condition, which clearly violate the mirror c symmetry. This is illustrated comparing Figs. 3(a) and 3(b) with the evolution of the $[1\bar{1}0]$ ED pattern between RT and 92 K. At this step, a careful rotation around $\vec{c}^*$, selecting the $[hk0]$ ED patterns with large h and k values, shows that, in our conditions of reflection, the Bragg peaks $00l$: $l=2n+1$ are scarcely visible but not null. By increasing T step by step up to room temperature, the intensity of the extra reflections remains unchanged between 90 and 200 K, it decreases from 200 to 265 K and, finally, disappears for $T>267$ K when keeping our working conditions constant. This transition temperature is probably underestimated, due to the heating of the sample under electron beam irradiation.

2. Combined NPD and HR-SXPD refinements at $T=350$ K and $T=100$ K

In agreement with the TEM results, high resolution x-ray and neutron powder diffraction indicate that a number of (hkl) Bragg reflections with odd l indices appear at low temperature. In the synchrotron x-ray diffraction pattern at 100 K, the strongest of these additional peaks is (221) whereas in the neutron data, two reflections indexed (221) and (223) in the hexagonal setting are the most clearly visible. The fact that these additional reflections appear at high value of the scattering vector (Q) and are present in the x-ray

TABLE I. Structural parameters of $SrMnO_3$, obtained by combined refinements of HRPD-ISIS, and ID31-ESRF neutron and synchrotron data. At 100 K, structural parameters have been constrained as $y(Sr_2)=1/3$, $y(Mn)=1/3$, $y(O_{12})=1/4$, $x(O22)=-3/2y(O21)$ and $x(O22)=-1/2y(O21)$. We also constrained the isotropic temperature factors to be the same for each chemical specie.

$T=350$ K: $P6_3/mmmc$ $a_h=b_h=5.461(1)$ Å $c=9.093(2)$ Å[a]					
	$Sr_1(2a)$	$Sr_2(4f)$	$Mn(4f)$	$O_1(6g)$	$O_2(6h)$
Position	(0,0,0)	(1/3,2/3,1/4)	(1/3,2/3,z)	(1/2,0,0)	($-x$,x,3/4)
			$z=0.61264(20)$		$x=0.81858(25)$
B_{iso}	0.67(8)	0.40(8)	0.26(7)	0.69(8)	0.40(7)
$T=100$ K: $C222_1$ $a=5.4435(1)$ Å $b\approx\sqrt{3}b_h=9.4211(2)$ Å $c=9.0630(1)$ Å[b]					
Atom	Wyck	x	y	z	B_{iso}
Sr1	4a	0.0096(8)	0	0	0.44(3)
Sr2	4b	0	1/3	1/4	0.44(3)
Mn	8c	–0.0123(8)	1/3	0.6131(2)	0.33(4)
O11	4a	0.5212(6)	0	0	0.64(4)
O12	8c	0.7712(6)	1/4	0.0085(5)	0.64(4)
O21	4b	0	–0.1798(2)	1/4	0.52(4)
O22	8c	0.2696(3)	0.0899(1)	0.2412(6)	0.52(4)

[a]NPD $\chi^2=8.47$, $R_{Bragg}=5.23\%$; HR-SXPD $\chi^2=6.91$, $R_{Bragg}=5.71\%$.
[b]NPD $\chi^2=4.37$, $R_{Bragg}=2.64\%$; HR-SXPD $\chi^2=2.51$, $R_{Bragg}=3.78\%$.

data, indicates their nuclear origin. At 350 K, the reflections are almost extinct but a close inspection of the diffraction pattern reveals a weak contribution even at this temperature. Nevertheless, their intensities at 350 K are too weak to determine an eventual change of structure. In this respect, the model of Battle *et al.*, with hexagonal symmetry $P6_3/mmc$, remains a valid approximation at high temperature. The extracted parameters from the combined refinement of x-ray and neutron data at 350 K, assuming $P6_3/mmc$ symmetry, are reported in Table I. At low temperature, this model is obviously invalid due to the presence of new reflections. Also, our preliminary study with medium resolution neutron diffraction as a function of temperature, indicates that the thermal parameters of some atoms, in particular O(1), increase when the temperature is lowered, suggesting that $P6_3/mmc$ is a pseudosymmetry. In agreement with our TEM results, NPD and HR-SXPD data are consistent with the absence of the c glide-plane symmetry operation. None of the maximal isotropy subgroups of order 2, as listed in the International Tables of crystallography,[21] is able to fit the data. The solution was found among isotropy subgroups of higher index, which are compatible with the Landau and Lifshitz conditions of the theory of second order phase transitions, as listed by Hatch and Stokes[22] or equivalently, by the program ISOTROPY.[23] The only solution fitting the data corresponds to the orthorhombic space group $C222_1$ with a supercell related to the hexagonal cell in the following way: $\mathbf{a}_o=\mathbf{a}_h$, $\mathbf{b}_o=\mathbf{a}_h+2\mathbf{b}_h$, $\mathbf{c}_o=\mathbf{c}_h$ (where o and h subscripts refer to the orthorhombic and hexagonal cells, respectively). This phase transition is a perfect example of pseudosymmetry problems since there is no direct indication of the orthorhombic symmetry from splitting of equivalent reflections or anisotropic broadening. The system remains metrically hexagonal within the very high resolution of our x-ray and neutron experiments; therefore in-plane lattice parameters were constrained accordingly in the refinements. This also indicate that the atomic displacements involved must be small enough to remain decoupled from the lattice strain.

The thermal parameters cannot be refined for all the crystallographic sites at low-temperatures. They have been constrained to be equal for atoms belonging to the same crystallographic site in the high temperature structure. The combined x-ray and neutron Rietveld refinement, presented in Fig. 4, is in excellent agreement with the data. Reliability factors and refined structural parameters are listed in Table I. It is important to note that a combined refinement is of crucial importance here, because of the difference in contrast in the x-ray and neutron experiments (O is a strong neutron scatterer, Mn neutron scattering length is negative).

The nature of the phase transition, involving all ions in the crystal, is difficult to comprehend without decomposing the respective atomic displacements. To that end, symmetry-adapted displacement modes were constructed using representation theory, as explained in the Appendix. The basis vectors describing these modes are reported in tables therein. Figure 5 graphically shows the modes associated to the irreducible representation Γ_5 corresponding to the structure observed at low temperature. Figures 5(a) and 5(b) represent individual modes while Fig. 5(c) shows the resulting displacements consistent with the final refinement of atomic positions. It appears that the structural transition involves a slight tilting of the corner-sharing Mn_2O_9 units composed of two face-sharing MnO_6 octahedra. This is coupled to a shear motion of Sr^{2+} cations in the ab plane. It is clear that the largest displacement is associated with the O(1) ions, explaining our preliminary results showing large thermal parameters for this site in the hexagonal setting. The sequential refinements of GEM data 1($1.5\ \text{K}<T<300\ \text{K}$) do not show

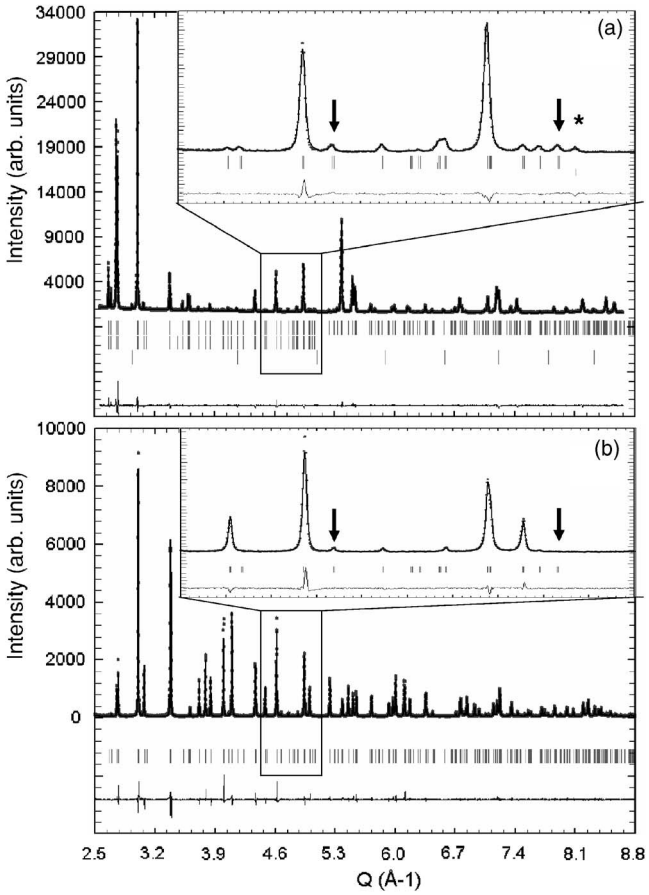

FIG. 4. Combined Rietveld refinement of the $SrMnO_3$ structure at 100 K with (a) NPD HRPD and (b) HR-SXPD ID-31 data collected on $SrMnO_3$ at $T=100$ K. For both patterns, the continuous line corresponds to the calculated pattern, while the lowest continuous line and tick marks indicate respectively the difference curve, and the position of Bragg reflections. For the NPD (a), the upper, middle and lower ticks represents the contribution from the nuclear scattering, the magnetic scattering, and the contribution from the Vanadium can (asterisk). Arrows indicate the position of the few reflections violating the extinction conditions of the high temperature space group $P6_3/mmc$.

any obvious discontinuity for most of the geometrical parameters of the structure, with the exception of the volume contraction. In particular, the Mn-O bond distances and angles within the Mn_2O_9 units are temperature independent. A clear signature of the structural transition is seen in the temperature dependence of some of the 180° Mn-O-Mn angles, which slightly decrease (by 2°) in the low temperature phase. The Raman data[16] must therefore be reinterpreted in the light of this rather subtle effect.

C. Magnetic structure

Below room temperature, additional Bragg reflections are observed in the powder neutron diffraction patterns, which can all be indexed with a propagation vector $\mathbf{k}=0$ with respect to the C-centered orthorhombic crystallographic unit cell. These reflections are clearly magnetic in origin since their intensities decrease rapidly as a function of the scattering vector Q, following the magnetic form factor. We note that magnetic scattering and the additional nuclear scattering related to the structural phase transition give rise to different contributions in the diffraction pattern, allowing treatment of both problems separately. Symmetry analysis of the magnetic structure has been performed using representation analysis and is detailed in the Appendix. The magnetic representation Γ is decomposed into the direct sum of irreducible representations

$$3\Gamma_1 + 3\Gamma_2 + 3\Gamma_3 + 3\Gamma_4, \tag{1}$$

where all $\Gamma_i(i=1,4)$ are one-dimensional representations of the little group G_k, which in this case ($\mathbf{k}=0$) is simply the crystallographic space group. Only two modes, ψ_7 or ψ_{10}, belonging to different representations Γ_3 and Γ_4, fit the experimental data. These modes give the same arrangement of spins with components along the a and b directions, respectively, and are equivalent in the hexagonal pseudo symmetry. In fact, these modes belong to a single irreducible representation when the analysis is performed in the hexagonal setting. For the same reason, it is impossible to determine the direction of the spins in the ab plane, and we have arbitrarily

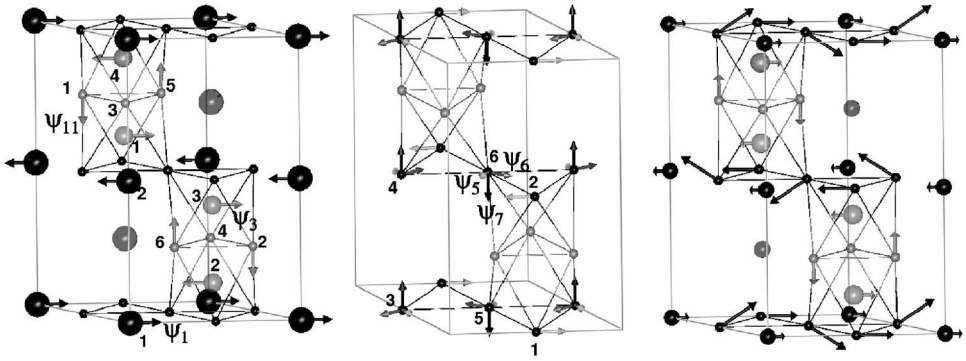

FIG. 5. Atomic displacement modes responsible for the structural phase transition in $SrMnO_3$. The arrows and the atom labels gives a graphical representation of the basis vectors of IR Γ_5 involved in the transition, which are given Table IV. (a) Displacement modes for Mn (medium sized grey spheres), Sr_1 (large black spheres), and O_2 (small grey spheres). (b) Displacement modes for O_1. (c) Resultant distortion from the linear combination $\Sigma_\lambda C_\lambda . \psi_\lambda$ of all basis functions: the refinement leads to $C_1>0$, $C_3<0$ and $C_{11}<0$ for Sr_1, Mn, and O_2, respectively. For O_1, the mixing coefficients can be constrained to have no component along (b), as $C_\alpha(\psi_5-\psi_6)+C_\beta\psi_7$.

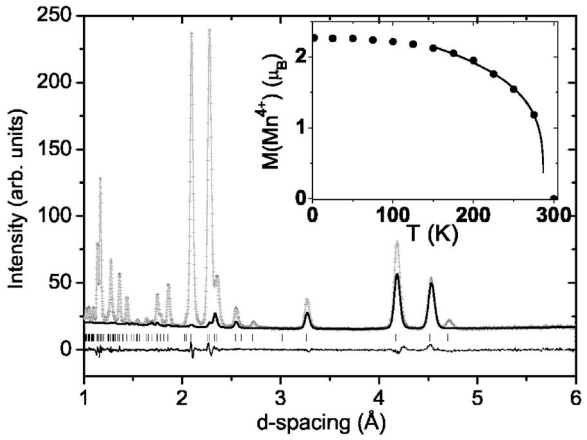

FIG. 6. Rietveld refinement of $SrMnO_3$ at $T=1.5$ K with GEM data collected. Data from a detector bank situated at 35° 2θ are shown. The experimental data points are shown as grey crosses while the calculated pattern is represented by a grey solid line. Contribution from magnetic scattering is plotted separately as a thick black solid line. The lowest continuous line shows the difference curve between data and refinement, while tick marks indicate the positions of Bragg reflections.

chosen to direct them along the *a* axis. The refinement, shown in Fig. 6, is of very good quality. The global user-weighted $\chi^2=1.30$, and the Bragg *R* factors are $R_{\text{nuc}}=2.44\%$, $R_{\text{nuc}}=2.29\%$, $R_{\text{nuc}}=2.54\%$, $R_{\text{mag}}=3.09\%$, $R_{\text{mag}}=2.39\%$, and $R_{\text{mag}}=7.58\%$ for patterns collected on the 34.96°, 63.62°, and 91.30° detectors banks, respectively. The magnetic structure is reported in Fig. 7. It corresponds to a simple antiferromagnetic arrangement with the magnetic moments of first neighbor Mn ions aligned antiparallel.

The most surprising finding is the value of the manganese magnetic moment extracted from our Rietveld refinements as a function of temperature, as shown in Fig. 6. For a quenched orbital contribution, the expected ordered moment for high spin Mn^{4+} ions is $3\mu_B$ per Mn ion but the observed value, saturating at 2.27(1) at low temperature, is reduced by 25%.

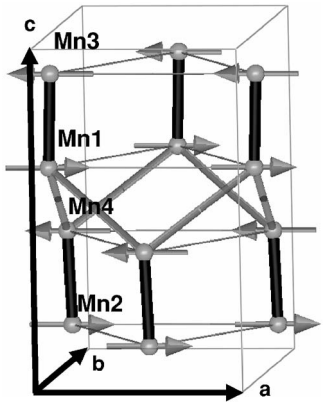

FIG. 7. Low temperature magnetic structure of $SrMnO_3$. It is described in the low temperature orthorhombic $C222_1$ cell. The Mn atoms are labeled according to the atoms given in Table V, translated in the zero unit cell.

IV. DISCUSSION

A. Structure

The nature of the structural phase transition and in particular its connection with the magnetic properties, is not immediately clear. The transition does not manifest as an abrupt decrease of the interatomic Mn-Mn distance, so that it cannot be related to exchange-striction. In the measured temperature range, the Mn-Mn distance decreases smoothly [$d_{\text{Mn-Mn}}=2.497(3)$ at 350 K and 2.485(2) at 100 K] following essentially the expected thermal expansion. Data collected on a finer temperature scale would be needed to exclude completely the presence of exchange striction in this material.

Even though it has not been precisely determined here, the structural phase transition temperature is certainly above 350 K and may coincide with the changes observed in magnetization at $T_s=380$ K. Therefore, it clearly has no connection with the onset of magnetic order at $T_N=286$ K. In fact, preliminary neutron measurements show that the structural transition temperature increases when Ca is substituted for Sr in the system, highlighting the critical role of ionic radius on the *A* site. From this, we conclude that the transition is primarily due to a steric effect. This probably influences indirectly the magnetic properties as follows. The distortion induces a small bending of the Mn-O-Mn angle between corner-sharing octahedra, which could reduce the electron transfer of the 3*d* electron between Mn pairs. This can accordingly enhance correlations associated to direct exchange interactions inside each pair below $T_s=380$ K, before the magnetic ordering is established below $T_N=286$ K.

B. Magnetism

The exchange topology of $SrMnO_3$ was introduced in Fig. 1. It is clear from that figure that the superexchange path J_2 is antiferromagnetic according to the Goodenough-Kanamori-Anderson (GKA) rules,[4,6] since Mn-O-Mn bond angle between corner-sharing MnO_6 octahedra is nearly 180°. However, GKA rules predict a ferromagnetic superexchange interaction for the path J_1 between Mn spins of face-sharing octahedra, since here, the Mn-O-Mn angle is nearly 90°. The observed antiferromagnetic arrangement between these Mn ions indicates that the exchange J_D through direct overlap of d orbitals, dominates over superexchange interactions. The sign of the direct exchange interaction depends on the interatomic distance between Mn ions, with shorter bonds favoring an antiferromagnetic arrangement. The effect of interatomic distances has been systematically studied in Mn intermetallic compounds.[13,14] In $R(\text{Mn,Fe})_6A$ (*R*: rare earth, *A*: Sn or Ge),[13] a crossover from ferromagnetic to antiferromagnetic interactions was clearly observed for distances below 2.61 Å, whereas in various solid solutions derived from MnSb,[14] that crossover is found for average Mn-Mn distances below 2.83 Å. A strong antiferromagnetic direct interaction arising from the small value of ~2.49 Å reported here for the Mn-Mn distance in $SrMnO_3$ is perfectly consistent with the trend seen in intermetallic compounds.

The ordered moment ($gS=2.27\mu_B$) in $SrMnO_3$ is small compared to that of other Mn^{4+}-based AF oxides such as

TABLE II. Representative matrices $d_i(g)$ for each irreducible representation Γ_i of the elements g belonging to the group of the wave vector $G_{\mathbf{k}}=P6_3/mmc$ for the space group $G=P6_3/mmc$ and $\mathbf{k}=(0\ 0\ 0)$.

IRs	Symmetry operators					
IT symbol	1	3+ 0,0,z	2 (0,0,1/2) 0,0,z	2 x,x,0	3− 0,0,z	6− (0,0,1/2) 0,0,z
	x,y,z	$-x$,$-y$,z+1/2	$-y$,$x-y$,z	y,$-x+y$,z+1/2	$-x+y$,$-x$,z	$x-y$,x,z+1/2
IT symbol	2 0,y,0	2 x,$-x$,1/4	6+ (0,0,1/2) 0,0,z	2 x,0,0	2 2x,x,1/4	2 x,2x,1/4
	y,x,$-z$	$-y$,$-x$,$-z-1/2$	$x-y$,$-y$,$-z$	$-x+y$,y,$-z-1/2$	$-x$,$-x+y$,$-z$	x,$x-y$,$-z-1/2$
IT symbol	−1 0,0,0	−3+ 0,0,z; 0,0,0	m x,y,1/4	m x,$-x$,z	−3− 0,0,z; 0,0,0	−6− 0,0,z; 0,0,1/4
	$-x$,$-y$,$-z$	x,y,$-z-1/2$	y,$-x+y$,$-z$	$-y$,$x-y$,$-z-1/2$	$x-y$,x,$-z$	$-x+y$,$-x$,$-z-1/2$
IT symbol	m 2x,x,2z	c x,x,z	−6+ 0,0,z; 0,0,1/4	m x,2x,z	c 0,y,z	c x,0,z
	$-y$,$-x$,z	y,x,z+1/2	$-x+y$,y,z	$x-y$,$-y$,z+1/2	x,$x-y$,z	$-x$,$-x+y$,z+1/2
Γ_1	1	1	1	1	1	1
	1	1	1	1	1	1
	1	1	1	1	1	1
	1	1	1	1	1	1
Γ_2	1	1	1	1	1	1
	1	1	1	1	1	1
	−1	−1	−1	−1	−1	−1
	−1	−1	−1	−1	−1	−1
Γ_3	1	1	1	1	1	1
	−1	−1	−1	−1	−1	−1
	1	1	1	1	1	1
	−1	−1	−1	−1	−1	−1
Γ_4	1	1	1	1	1	1
	−1	−1	−1	−1	−1	−1
	−1	−1	−1	−1	−1	−1
	1	1	1	1	1	1
Γ_5	$\begin{pmatrix}1 & 0\\ 0 & 1\end{pmatrix}$	$\begin{pmatrix}1 & 0\\ 0 & 1\end{pmatrix}$	$\begin{pmatrix}-\frac{1}{2} & \frac{\sqrt{3}}{2}\\ -\frac{\sqrt{3}}{2} & -\frac{1}{2}\end{pmatrix}$	$\begin{pmatrix}-\frac{1}{2} & \frac{\sqrt{3}}{2}\\ -\frac{\sqrt{3}}{2} & -\frac{1}{2}\end{pmatrix}$	$\begin{pmatrix}-\frac{1}{2} & -\frac{\sqrt{3}}{2}\\ \frac{\sqrt{3}}{2} & -\frac{1}{2}\end{pmatrix}$	$\begin{pmatrix}-\frac{1}{2} & -\frac{\sqrt{3}}{2}\\ \frac{\sqrt{3}}{2} & -\frac{1}{2}\end{pmatrix}$
	$\begin{pmatrix}-\frac{1}{2} & -\frac{\sqrt{3}}{2}\\ -\frac{\sqrt{3}}{2} & \frac{1}{2}\end{pmatrix}$	$\begin{pmatrix}-\frac{1}{2} & -\frac{\sqrt{3}}{2}\\ -\frac{\sqrt{3}}{2} & \frac{1}{2}\end{pmatrix}$	$\begin{pmatrix}1 & 0\\ 0 & -1\end{pmatrix}$	$\begin{pmatrix}1 & 0\\ 0 & -1\end{pmatrix}$	$\begin{pmatrix}-\frac{1}{2} & \frac{\sqrt{3}}{2}\\ \frac{\sqrt{3}}{2} & \frac{1}{2}\end{pmatrix}$	$\begin{pmatrix}-\frac{1}{2} & \frac{\sqrt{3}}{2}\\ \frac{\sqrt{3}}{2} & \frac{1}{2}\end{pmatrix}$
	$\begin{pmatrix}-1 & 0\\ 0 & -1\end{pmatrix}$	$\begin{pmatrix}-1 & 0\\ 0 & -1\end{pmatrix}$	$\begin{pmatrix}\frac{1}{2} & -\frac{\sqrt{3}}{2}\\ \frac{\sqrt{3}}{2} & \frac{1}{2}\end{pmatrix}$	$\begin{pmatrix}\frac{1}{2} & -\frac{\sqrt{3}}{2}\\ \frac{\sqrt{3}}{2} & \frac{1}{2}\end{pmatrix}$	$\begin{pmatrix}\frac{1}{2} & \frac{\sqrt{3}}{2}\\ -\frac{\sqrt{3}}{2} & \frac{1}{2}\end{pmatrix}$	$\begin{pmatrix}\frac{1}{2} & \frac{\sqrt{3}}{2}\\ -\frac{\sqrt{3}}{2} & \frac{1}{2}\end{pmatrix}$
	$\begin{pmatrix}\frac{1}{2} & \frac{\sqrt{3}}{2}\\ \frac{\sqrt{3}}{2} & -\frac{1}{2}\end{pmatrix}$	$\begin{pmatrix}\frac{1}{2} & \frac{\sqrt{3}}{2}\\ \frac{\sqrt{3}}{2} & -\frac{1}{2}\end{pmatrix}$	$\begin{pmatrix}-1 & 0\\ 0 & 1\end{pmatrix}$	$\begin{pmatrix}-1 & 0\\ 0 & 1\end{pmatrix}$	$\begin{pmatrix}\frac{1}{2} & -\frac{\sqrt{3}}{2}\\ -\frac{\sqrt{3}}{2} & -\frac{1}{2}\end{pmatrix}$	$\begin{pmatrix}\frac{1}{2} & -\frac{\sqrt{3}}{2}\\ -\frac{\sqrt{3}}{2} & -\frac{1}{2}\end{pmatrix}$
Γ_6	$\begin{pmatrix}1 & 0\\ 0 & 1\end{pmatrix}$	$\begin{pmatrix}1 & 0\\ 0 & 1\end{pmatrix}$	$\begin{pmatrix}-\frac{1}{2} & \frac{\sqrt{3}}{2}\\ -\frac{\sqrt{3}}{2} & -\frac{1}{2}\end{pmatrix}$	$\begin{pmatrix}-\frac{1}{2} & \frac{\sqrt{3}}{2}\\ -\frac{\sqrt{3}}{2} & -\frac{1}{2}\end{pmatrix}$	$\begin{pmatrix}-\frac{1}{2} & -\frac{\sqrt{3}}{2}\\ \frac{\sqrt{3}}{2} & -\frac{1}{2}\end{pmatrix}$	$\begin{pmatrix}-\frac{1}{2} & -\frac{\sqrt{3}}{2}\\ \frac{\sqrt{3}}{2} & -\frac{1}{2}\end{pmatrix}$

TABLE II. (*Continued.*)

IRs	Symmetry operators					
IT symbol	1	3+ 0,0,z	2 (0,0,1/2) 0,0,z	2 x,x,0	3− 0,0,z	6− (0,0,1/2) 0,0,z
	x,y,z	$-x$,$-y$,z+1/2	$-y$,$x-y$,z	y,$-x+y$,z+1/2	$-x+y$,$-x$,z	$x-y$,x,z+1/2
IT symbol	2 0,y,0	2 x,$-x$,1/4	6+ (0,0,1/2) 0,0,z	2 x,0,0	2 2x,x,1/4	2 x,2x,1/4
	y,x,$-z$	$-y$,$-x$,$-z-1/2$	$x-y$,$-y$,$-z$	$-x+y$,y,$-z-1/2$	$-x$,$-x+y$,$-z$	x,$x-y$,$-z-1/2$
IT symbol	−1 0,0,0	−3+ 0,0,z; 0,0,0	m x,y,1/4	m x,$-x$,z	−3− 0,0,z; 0,0,0	−6− 0,0,z; 0,0,1/4
	$-x$,$-y$,$-z$	x,y,$-z-1/2$	y,$-x+y$,$-z$	$-y$,$x-y$,$-z-1/2$	$x-y$,x,$-z$	$-x+y$,$-x$,$-z-1/2$
IT symbol	m 2x,x,2z	c x,x,z	−6+ 0,0,z; 0,0,1/4	m x,2x,z	c 0,y,z	c x,0,z
	$-y$,$-x$,z	y,x,z+1/2	$-x+y$,y,z	$x-y$,$-y$,z+1/2	x,$x-y$,z	$-x$,$-x+y$,z+1/2
	$\begin{pmatrix} -\frac{1}{2} & -\frac{\sqrt{3}}{2} \\ -\frac{\sqrt{3}}{2} & \frac{1}{2} \end{pmatrix}$	$\begin{pmatrix} -\frac{1}{2} & -\frac{\sqrt{3}}{2} \\ -\frac{\sqrt{3}}{2} & \frac{1}{2} \end{pmatrix}$	$\begin{pmatrix} 1 & 0 \\ 0 & -1 \end{pmatrix}$	$\begin{pmatrix} 1 & 0 \\ 0 & -1 \end{pmatrix}$	$\begin{pmatrix} -\frac{1}{2} & \frac{\sqrt{3}}{2} \\ \frac{\sqrt{3}}{2} & \frac{1}{2} \end{pmatrix}$	$\begin{pmatrix} -\frac{1}{2} & \frac{\sqrt{3}}{2} \\ \frac{\sqrt{3}}{2} & \frac{1}{2} \end{pmatrix}$
	$\begin{pmatrix} 1 & 0 \\ 0 & 1 \end{pmatrix}$	$\begin{pmatrix} 1 & 0 \\ 0 & 1 \end{pmatrix}$	$\begin{pmatrix} -\frac{1}{2} & \frac{\sqrt{3}}{2} \\ -\frac{\sqrt{3}}{2} & -\frac{1}{2} \end{pmatrix}$	$\begin{pmatrix} -\frac{1}{2} & \frac{\sqrt{3}}{2} \\ -\frac{\sqrt{3}}{2} & -\frac{1}{2} \end{pmatrix}$	$\begin{pmatrix} -\frac{1}{2} & -\frac{\sqrt{3}}{2} \\ \frac{\sqrt{3}}{2} & -\frac{1}{2} \end{pmatrix}$	$\begin{pmatrix} -\frac{1}{2} & -\frac{\sqrt{3}}{2} \\ \frac{\sqrt{3}}{2} & -\frac{1}{2} \end{pmatrix}$
	$\begin{pmatrix} -\frac{1}{2} & -\frac{\sqrt{3}}{2} \\ -\frac{\sqrt{3}}{2} & \frac{1}{2} \end{pmatrix}$	$\begin{pmatrix} -\frac{1}{2} & -\frac{\sqrt{3}}{2} \\ -\frac{\sqrt{3}}{2} & \frac{1}{2} \end{pmatrix}$	$\begin{pmatrix} 1 & 0 \\ 0 & -1 \end{pmatrix}$	$\begin{pmatrix} 1 & 0 \\ 0 & -1 \end{pmatrix}$	$\begin{pmatrix} -\frac{1}{2} & \frac{\sqrt{3}}{2} \\ \frac{\sqrt{3}}{2} & \frac{1}{2} \end{pmatrix}$	$\begin{pmatrix} -\frac{1}{2} & \frac{\sqrt{3}}{2} \\ \frac{\sqrt{3}}{2} & \frac{1}{2} \end{pmatrix}$

$BaMnO_3$ (Ref. 9), $CaMnO_3$ (Ref. 24), and $CaMn_2O_4$.[25] This moment reduction can have two origins: zero point fluctuations of the AF ground state, which are enhanced in compounds with reduced dimensionality or frustration, and covalency effects. The role of covalency in $SrMnO_3$ is definitively important, as recently pointed out in Ref. 26

As for many high spin systems, $CaMnO_3$ shows the rather classical behavior expected from an Heisenberg system with isotropic superexchange interactions. The ordered moment observed is reduced, due to oxygen deficiency, since the moment value extrapolated for stoichiometric $CaMnO_3$ is $gS=3\mu_B$.[24] Quantum fluctuations are obviously more important in the layered $CaMn_2O_4$ manganites,[25] but still, the moment reduction induced by the lower dimensionality, is not as large as that observed in $SrMnO_3$. Similarly, the quasi-one-dimensional hexagonal system $BaMnO_3$ (2L-polytype structure) should also have a significantly reduced ordered moment, but in fact, the reported value is saturated ($gS=3\pm0.3\mu_B$).[9] The dependence of the moment value in different materials seems to be controlled by the degree of exchange frustration: in $BaMnO_3$, the frustration between direct exchange and superexchange across face-sharing octahedra is released compared to $SrMnO_3$, with a bigger direct antiferromagnetic exchange interaction expected from a shorter Mn-Mn distance ($d_{\text{Mn-Mn}}=2.40$ Å). The trend is confirmed for $Ba_{0.1}Sr_{0.9}MnO_{2.96}$, where the reported ordered moment is intermediate between $SrMnO_3$ and $BaMnO_3$ ($gS=2.41\mu_B$).

From the present data and the comparison with other materials, we therefore suggest that the 3D-Heisenberg/SE picture does not fully hold in $SrMnO_3$ due to a competition between SE and direct exchange interactions, enhanced by short Mn-Mn distances in face-sharing octahedra. Instead of isolated high spin Mn^{4+} ions, the proper magnetic unit should be considered as Mn_2O_9 pairs. The problem is similar to the loss of V^{3+} ion identity[27] in the prototype material V_2O_3, which shows pairs of face-sharing VO_6 octahedra interconnected by the edges in the corrundum structure. In that case, the localized-electron unit in the antiferromagnetic insulating ground state has been identified as the nearest-neighbor pairs, with the electrons delocalized within a pair. Later, this has been thoroughly confirmed by theoretical investigation of effective spin/orbital Hamiltonians.[28]

V. CONCLUSION

In summary, we have shown that a structural transition does take place in $SrMnO_3$, but that this occurs at much higher temperature than previously reported from Raman scattering,[16] and is probably correlated with the transition observed in magnetization at ~380 K. The structural transformation does not correspond to a change of polytype, but to a subtle distortion within the 4L structure lowering the hexagonal $P6_3/mmc$ symmetry to an orthorhombic pseudosymmetry ($C222_1$), which preserves the hexagonal metrics. The structural transition seems to be primarily due to steric effects and is found to affect only indirectly the magnetic exchange. NPD reveals that $SrMnO_3$ has a reduced moment at low temperatures, possibly arising from the presence of delocalized electrons within Mn_2O_9 pairs. This finding de-

TABLE III. Continuation of Table II.

IRs	Symmetry operators					
IT symbol	1	3+ 0,0,z	2 (0,0,1/2) 0,0,z	2 x,x,0	3− 0,0,z	6− (0,0,1/2) 0,0,z
	x,y,z	$-x$,$-y$,$z+1/2$	$-y$,$x-y$,z	y,$-x+y$,$z+1/2$	$-x+y$,$-x$,z	$x-y$,x,$z+1/2$
IT symbol	2 0,y,0	2 x,$-x$,1/4	6+ (0,0,1/2) 0,0,z	2 x,0,0	2 2x,x,1/4	2 x,2x,1/4
	y,x,$-z$	$-y$,$-x$,$-z-1/2$	$x-y$,$-y$,$-z$	$-x+y$,y,$-z-1/2$	$-x$,$-x+y$,$-z$	x,$x-y$,$-z-1/2$
IT symbol	−1 0,0,0	−3+ 0,0,z; 0,0,0	m x,y,1/4	m x,$-x$,z	−3− 0,0,z; 0,0,0	−6− 0,0,z; 0,0,1/4
	$-x$,$-y$,$-z$	x,y,$-z-1/2$	y,$-x+y$,$-z$	$-y$,$x-y$,$-z-1/2$	$x-y$,x,$-z$	$-x+y$,$-x$,$-z-1/2$
IT symbol	m 2x,x,2z	c x,x,z	−6+ 0,0,z; 0,0,1/4	m x,2x,z	c 0,y,z	c x,0,z
	$-y$,$-x$,z	y,x,$z+1/2$	$-x+y$,y,z	$x-y$,$-y$,$z+1/2$	x,$x-y$,z	$-x$,$-x+y$,$z+1/2$
Γ_7	1	−1	1	−1	1	−1
	1	−1	1	−1	1	−1
	1	−1	1	−1	1	−1
	1	−1	1	−1	1	−1
Γ_8	1	−1	1	−1	1	−1
	1	−1	1	−1	1	−1
	−1	1	−1	1	−1	1
	−1	1	−1	1	−1	1
Γ_9	1	−1	1	−1	1	−1
	−1	1	−1	1	−1	1
	1	−1	1	−1	1	−1
	−1	1	−1	1	−1	1
Γ_{10}	1	−1	1	−1	1	−1
	−1	1	−1	1	−1	1
	−1	1	−1	1	−1	1
	1	−1	1	−1	1	−1
Γ_{11}	$\begin{pmatrix}1 & 0\\ 0 & 1\end{pmatrix}$	$\begin{pmatrix}-1 & 0\\ 0 & -1\end{pmatrix}$	$\begin{pmatrix}-\frac{1}{2} & \frac{\sqrt{3}}{2}\\ -\frac{\sqrt{3}}{2} & -\frac{1}{2}\end{pmatrix}$	$\begin{pmatrix}\frac{1}{2} & -\frac{\sqrt{3}}{2}\\ \frac{\sqrt{3}}{2} & \frac{1}{2}\end{pmatrix}$	$\begin{pmatrix}-\frac{1}{2} & -\frac{\sqrt{3}}{2}\\ \frac{\sqrt{3}}{2} & -\frac{1}{2}\end{pmatrix}$	$\begin{pmatrix}\frac{1}{2} & \frac{\sqrt{3}}{2}\\ -\frac{\sqrt{3}}{2} & \frac{1}{2}\end{pmatrix}$
	$\begin{pmatrix}-\frac{1}{2} & -\frac{\sqrt{3}}{2}\\ -\frac{\sqrt{3}}{2} & \frac{1}{2}\end{pmatrix}$	$\begin{pmatrix}\frac{1}{2} & \frac{\sqrt{3}}{2}\\ \frac{\sqrt{3}}{2} & -\frac{1}{2}\end{pmatrix}$	$\begin{pmatrix}1 & 0\\ 0 & -1\end{pmatrix}$	$\begin{pmatrix}-1 & 0\\ 0 & 1\end{pmatrix}$	$\begin{pmatrix}-\frac{1}{2} & \frac{\sqrt{3}}{2}\\ \frac{\sqrt{3}}{2} & \frac{1}{2}\end{pmatrix}$	$\begin{pmatrix}\frac{1}{2} & -\frac{\sqrt{3}}{2}\\ -\frac{\sqrt{3}}{2} & -\frac{1}{2}\end{pmatrix}$
	$\begin{pmatrix}-1 & 0\\ 0 & -1\end{pmatrix}$	$\begin{pmatrix}1 & 0\\ 0 & 1\end{pmatrix}$	$\begin{pmatrix}\frac{1}{2} & -\frac{\sqrt{3}}{2}\\ \frac{\sqrt{3}}{2} & \frac{1}{2}\end{pmatrix}$	$\begin{pmatrix}-\frac{1}{2} & \frac{\sqrt{3}}{2}\\ -\frac{\sqrt{3}}{2} & -\frac{1}{2}\end{pmatrix}$	$\begin{pmatrix}\frac{1}{2} & \frac{\sqrt{3}}{2}\\ -\frac{\sqrt{3}}{2} & \frac{1}{2}\end{pmatrix}$	$\begin{pmatrix}-\frac{1}{2} & -\frac{\sqrt{3}}{2}\\ \frac{\sqrt{3}}{2} & -\frac{1}{2}\end{pmatrix}$
	$\begin{pmatrix}\frac{1}{2} & \frac{\sqrt{3}}{2}\\ \frac{\sqrt{3}}{2} & -\frac{1}{2}\end{pmatrix}$	$\begin{pmatrix}-\frac{1}{2} & -\frac{\sqrt{3}}{2}\\ -\frac{\sqrt{3}}{2} & \frac{1}{2}\end{pmatrix}$	$\begin{pmatrix}-1 & 0\\ 0 & 1\end{pmatrix}$	$\begin{pmatrix}1 & 0\\ 0 & -1\end{pmatrix}$	$\begin{pmatrix}\frac{1}{2} & -\frac{\sqrt{3}}{2}\\ -\frac{\sqrt{3}}{2} & -\frac{1}{2}\end{pmatrix}$	$\begin{pmatrix}-\frac{1}{2} & \frac{\sqrt{3}}{2}\\ \frac{\sqrt{3}}{2} & \frac{1}{2}\end{pmatrix}$
Γ_{12}	$\begin{pmatrix}1 & 0\\ 0 & 1\end{pmatrix}$	$\begin{pmatrix}-1 & 0\\ 0 & -1\end{pmatrix}$	$\begin{pmatrix}-\frac{1}{2} & \frac{\sqrt{3}}{2}\\ -\frac{\sqrt{3}}{2} & -\frac{1}{2}\end{pmatrix}$	$\begin{pmatrix}\frac{1}{2} & -\frac{\sqrt{3}}{2}\\ \frac{\sqrt{3}}{2} & \frac{1}{2}\end{pmatrix}$	$\begin{pmatrix}-\frac{1}{2} & -\frac{\sqrt{3}}{2}\\ \frac{\sqrt{3}}{2} & -\frac{1}{2}\end{pmatrix}$	$\begin{pmatrix}\frac{1}{2} & \frac{\sqrt{3}}{2}\\ -\frac{\sqrt{3}}{2} & \frac{1}{2}\end{pmatrix}$

TABLE III. (*Continued.*)

IRs	Symmetry operators					
IT symbol	1	3+ 0,0,z	2 (0,0,1/2) 0,0,z	2 x,x,0	3– 0,0,z	6– (0,0,1/2) 0,0,z
	x,y,z	$-x$,$-y$,z+1/2	$-y$,$x-y$,z	y,$-x+y$,z+1/2	$-x+y$,$-x$,z	$x-y$,x,z+1/2
IT symbol	2 0,y,0	2 x,$-x$,1/4	6+ (0,0,1/2) 0,0,z	2 x,0,0	2 2x,x,1/4	2 x,2x,1/4
	y,x,$-z$	$-y$,$-x$,$-z$−1/2	$x-y$,$-y$,$-z$	$-x+y$,y,$-z$−1/2	$-x$,$-x+y$,$-z$	x,$x-y$,$-z$−1/2
IT symbol	−1 0,0,0	−3+ 0,0,z; 0,0,0	m x,y,1/4	m x,$-x$,z	−3– 0,0,z; 0,0,0	−6– 0,0,z; 0,0,1/4
	$-x$,$-y$,$-z$	x,y,$-z$−1/2	y,$-x+y$,$-z$	$-y$,$x-y$,$-z$−1/2	$x-y$,x,$-z$	$-x+y$,$-x$,$-z$−1/2
IT symbol	m 2x,x,2z	c x,x,z	−6+ 0,0,z; 0,0,1/4	m x,2x,z	c 0,y,z	c x,0,z
	$-y$,$-x$,z	y,x,z+1/2	$-x+y$,y,z	$x-y$,$-y$,z+1/2	x,$x-y$,z	$-x$,$-x+y$,z+1/2
	$\begin{pmatrix}1 & 0\\ 0 & 1\end{pmatrix}$	$\begin{pmatrix}-1 & 0\\ 0 & -1\end{pmatrix}$	$\begin{pmatrix}-\frac{1}{2} & \frac{\sqrt{3}}{2}\\ -\frac{\sqrt{3}}{2} & -\frac{1}{2}\end{pmatrix}$	$\begin{pmatrix}\frac{1}{2} & -\frac{\sqrt{3}}{2}\\ \frac{\sqrt{3}}{2} & \frac{1}{2}\end{pmatrix}$	$\begin{pmatrix}-\frac{1}{2} & -\frac{\sqrt{3}}{2}\\ \frac{\sqrt{3}}{2} & -\frac{1}{2}\end{pmatrix}$	$\begin{pmatrix}\frac{1}{2} & \frac{\sqrt{3}}{2}\\ -\frac{\sqrt{3}}{2} & \frac{1}{2}\end{pmatrix}$
	$\begin{pmatrix}-\frac{1}{2} & -\frac{\sqrt{3}}{2}\\ -\frac{\sqrt{3}}{2} & \frac{1}{2}\end{pmatrix}$	$\begin{pmatrix}\frac{1}{2} & \frac{\sqrt{3}}{2}\\ \frac{\sqrt{3}}{2} & -\frac{1}{2}\end{pmatrix}$	$\begin{pmatrix}1 & 0\\ 0 & -1\end{pmatrix}$	$\begin{pmatrix}-1 & 0\\ 0 & 1\end{pmatrix}$	$\begin{pmatrix}-\frac{1}{2} & \frac{\sqrt{3}}{2}\\ \frac{\sqrt{3}}{2} & \frac{1}{2}\end{pmatrix}$	$\begin{pmatrix}\frac{1}{2} & -\frac{\sqrt{3}}{2}\\ -\frac{\sqrt{3}}{2} & -\frac{1}{2}\end{pmatrix}$

TABLE IV. Basis functions ψ_i of representation Γ_5, for each crystallographic site of $SrMnO_3$.

Atom: $Sr1_1$ at position (0, 0, 0)

SYMM	x,y,z	$-x$,$-y$,z+1/2	
Atoms:	$Sr1_1$	$Sr1_2$	
Ψ_1	(1 0 0)	(−1 0 0)	
Ψ_2	(−1 −2 0)	(1 2 0)	

Atom: Mn_1 at position $\left(\frac{1}{3}\ \frac{2}{3}\ 0.6129\right)$

SYMM	x,y,z	$-x$,$-y$,z+1/2	y,x,$-z$	$-y$,$-x$,$-z$+1/2
Atoms:	Mn_1	Mn_2	Mn_3	Mn_4
Ψ_3	(1 0 0)	(−1 0 0)	(1 0 0)	(−1 0 0)
Ψ_4	(−1 −2 0)	(1 2 0)	(−1 −2 0)	(1 2 0)

Atom: $O1_1$ at position $\left(\frac{1}{2}\ 0\ 0\right)$

SYMM	x,y,z	$-x$,$-y$,z+1/2	$-y$,$x-y$,z	y,$-x+y$,z+1/2	$-x+y$,$-x$,z	$x-y$,x,z+1/2
Atoms:	$O1_1$	$O1_2$	$O1_3$	$O1_4$	$O1_5$	$O1_6$
Ψ_5	(2 0 0)	(−2 0 0)	(0 −1 0)	(0 1 0)	(1 1 0)	(−1 −1 0)
Ψ_6	(0 0 0)	(0 0 0)	(−2 −1 0)	(2 1 0)	(−1 1 0)	(1 −1 0)
Ψ_7	(0 0 0)	(0 0 0)	(0 0 1)	(0 0 1)	(0 0 −1)	(0 0 −1)
Ψ_8	(0 0 0)	(0 0 0)	(0 −1 0)	(0 1 0)	(−1 −1 0)	(1 1 0)
Ψ_9	(0 0 0)	(0 0 0)	(0 1 0)	(0 −1 0)	(1 1 0)	(−1 −1 0)
Ψ_{10}	(0 0 2)	(0 0 2)	(0 0 −1)	(0 0 −1)	(0 0 −1)	(0 0 −1)

Atom $O2_1$ at position $\left(-0.8209\ 0.8209\ \frac{3}{4}\right)$

SYMM	x,y,z	$-x$,$-y$,z+1/2	$-y$,$x-y$,z	y,$-x+y$,z+1/2	$-x+y$,$-x$,z	$x-y$,x,z+1/2
Atoms:	$O2_1$	$O2_2$	$O2_3$	$O2_4$	$O2_5$	$O2_6$
Ψ_{11}	(0 0 1)	(0 0 1)	(0 0 0)	(0 0 0)	(0 0 −1)	(0 0 −1)
Ψ_{12}	(0 0 1)	(0 0 1)	(0 0 −2)	(0 0 −2)	(0 0 1)	(0 0 1)

TABLE V. IRs for the little group $G_{\mathbf{k}}=G$ of $G=C222_1$ and $\mathbf{k}=(0,0,0)$ and SBF for the orbit of the starting atom Mn_1 at position the (−0.0120 0.3333 0.6130).

		IRs		
IT symbol	1	2 (0,0,1/2) 0,0,z	2 0,y,1/4	2 x,0,0
$G_{\mathbf{k}}$	x,y,z	$-x,-y,z+1/2$	$-x,y,-z+1/2$	$x,-y,-z$
Γ_1	1	1	1	1
Γ_2	1	1	−1	−1
Γ_3	1	−1	1	−1
Γ_4	1	−1	−1	1

		SBF			
Atoms		Mn_1	Mn_2	Mn_3	Mn_4
Position		x,y,z	$-x,-y,z+1/2$	$-x,y,-z+1/2$	$x,-y,-z$
	ψ_1	(1 0 0)	(−1 0 0)	(−1 0 0)	(1 0 0)
Γ_1	ψ_2	(0 1 0)	(0 −1 0)	(0 1 0)	(0 −1 0)
	ψ_3	(0 0 1)	(0 0 1)	(0 0 −1)	(0 0 −1)
	ψ_3	(1 0 0)	(−1 0 0)	(1 0 0)	(−1 0 0)
Γ_2	ψ_4	(0 1 0)	(0 −1 0)	(0−1 0)	(0 1 0)
	ψ_5	(0 0 1)	(0 0 1)	(0 0 1)	(0 0 1)
	ψ_6	(1 0 0)	(1 0 0)	(−1 0 0)	(−1 0 0)
Γ_3	ψ_7	(0 1 0)	(0 1 0)	(0 1 0)	(0 1 0)
	ψ_8	(0 0 1)	(0 0 −1)	(0 0 −1)	(0 0 1)
	ψ_9	(1 0 0)	(1 0 0)	(1 0 0)	(1 0 0)
Γ_4	$\psi_1 0$	(0 1 0)	(0 1 0)	(0−1 0)	(0 −1 0)
	$\psi_1 1$	(0 0 1)	(0 0 −1)	(0 0 1)	(0 0 −1)

serves confirmation from theoretical studies of the electronic structure.

APPENDIX: SYMMETRY ANALYSIS OF THE STRUCTURAL AND MAGNETIC TRANSITIONS

The symmetry properties of the low temperature structure of $SrMnO_3$ have been determined by representation analysis. The atomic positions are written

$$\mathbf{r}_{ni} = \mathbf{r}_i^0 + \mathbf{u}_{ni} \tag{A1}$$

for atoms in crystallographic cells indexed by $\mathbf{R}_n$ that were at average positions $\mathbf{r}_i^0$ in the high temperature phase, which are now displaced by vectors $\mathbf{u}_{ni}$. These displacement vectors are decomposed with the Fourier sum

$$\mathbf{u}_{ni} = \sum_{\mathbf{k}} \mathbf{u}_{\mathbf{k}}^i e^{2i\pi\mathbf{k}\cdot\mathbf{R}_n} + \mathbf{u}_{\mathbf{k}}^{i*} e^{-2i\pi\mathbf{k}\cdot\mathbf{R}_n}, \tag{A2}$$

where $\mathbf{k}$ is the wave vector characterizing how the translational symmetry is broken at the transition.

The symmetry relations between the vectors $\mathbf{u}_{\mathbf{k}}^i$ for atoms of the same crystallographic orbit are obtained for each irreducible representation (IR) Γ_ν using the projection operator

$$\hat{P}^\nu = \left\{ \sum_{g\in G_{\mathbf{k}}} D_{\lambda\mu}^{*\nu}(g)\hat{g} \right\}. \tag{A3}$$

The sum is over the symmetry elements g of the little group transforming $\mathbf{k}$ into an equivalent wave vector. $D_{\lambda\mu}^{*\nu}(g)$ are elements of the matrix representation of g for the IR ν. This operator projects an arbitrary set of displacement components on atoms of a crystallographic orbit of multiplicity σ, onto symmetrized basis functions (SBFs). We conveniently write these SBFs as $\Psi_\lambda^\nu = \sum_{i=1\cdots\sigma,\alpha=x,y,z}^{\oplus} a_{i\alpha}\mathbf{e}_{i\alpha}$, where $\{\mathbf{e}_{i\alpha}\}$ represents the displacement vectors components on an atom i in the direction α. An arbitrary set of linearly independent SBFs are chosen from all the constructed ones. Working out with SBFs belonging to a single IR is equivalent to assume a distortion compatible with a second order transition.

In our case, the propagation vector observed experimentally is $\mathbf{k}=(0,0,0)$, a special case where the complex Fourier component $u_{\mathbf{k}}^i$ identifies with the real displacement $\mathbf{u}_{ni}$. As always with $\mathbf{k}=(0\,0\,0)$, all the symmetry elements of $P6_3/mmc$ leave $\mathbf{k}$ invariant, hence, $G_{\mathbf{k}}$ coincides with the space group $P6_3/mmc$. IRs and basis functions were obtained using the program BASIREPS. In our case, however, the program outputs eight real one-dimensional representations and four two-dimensional complex representations. The SBF being expected to be real, it is desirable to transform the complex representations into real using an appropriate unitary similarity transformation matrix U, for which $U^{-1}=(U^*)^T$ before projection. Using

$$U = \frac{1}{2\sqrt{(2-\sqrt{3})^2+1}} \begin{pmatrix} 2-\sqrt{3} & 1 \\ 1 & -2+\sqrt{3} \end{pmatrix} \begin{pmatrix} 1+i & -1+i \\ 1-i & -1-i \end{pmatrix} \tag{A4}$$

real matrices $d(g)=U^{-1}D(g)U$ for the IRs $\Gamma_5,\Gamma_6,\Gamma_{11},\Gamma_{12}$ have been thus obtained from the complex matrices $D(g)$, which are output by BASIREPS (see Tables II and III).

The projection of the SBF is illustrated for the two-dimensional representation labeled Γ_5, which correspond to the IR actually chosen at the phase transition in $SrMnO_3$. With the special choice of unitary transform, we could straightforwardly double check that the symmetry modes associated to the transition from $P6_3/mmc$ to $C222_1$ and given by the program SYMMODES of the Bilbao crystallographic server[29] indeed correspond to a subsets of the SBF calculated for the IR Γ_5 by BASIREPS (see Table IV).

Representation analysis is more general, and also applies to other type of phase transitions where atoms acquire a new scalar, vectorial, or tensorial property in the low-symmetry phase. Instead of dealing with atomic displacements (polar vectors) in the case of structural transitions, we can indeed deal with the appearance of a magnetic moment to treat the case of magnetic transitions:

$$\mu_{ni} = \mathbf{S}_{\mathbf{k}}^{i} e^{2i\pi \mathbf{k} R_n} + \mathbf{S}_{\mathbf{k}}^{i*} e^{-2i\pi \mathbf{k} R_n}. \quad \text{(A5)}$$

The only change in the orthogonalization procedure and the construction of the SBF summarizing this time the symmetry relation of the Fourier components $S_{\mathbf{k}}^{i}$, is the action of the space group operation g in Eq. (A3), which is different for axial and polar vectors. We similarly obtained the symmetry analysis of the possible magnetic structure of $SrMnO_3$, which is summarized in Table V.

[1] E. Dagotto, T. Hotta, and A. Moreoa, Phys. Rep. **344**, 1 (2001).
[2] J. Orenstein and A. Millis, Science **288**, 468 (2000).
[3] A. Imada, M. Fujimori, and Y. Tokura, Rev. Mod. Phys. **70**, 1039 (1998).
[4] J. B. Goodenough, Phys. Rev. **100**, 564 (1955).
[5] P. Anderson, Phys. Rev. **115**, 2 (1959).
[6] J. Kanamori, J. Phys. Chem. Solids **10**, 87 (1959).
[7] T. E. Mason, B. D. Gaulin, and M. F. Collins, Phys. Rev. B **39**, 586 (1989).
[8] A. Harrison, M. F. Collins, J. Abu-Dayyeh, and C. V. Stager, Phys. Rev. B **43**, 679 (1991).
[9] A. N. Christensen and G. Ollivier, J. Solid State Chem. **4**, 131 (1972).
[10] T. Negas and R. S. Roth, J. Solid State Chem. **1**, 409 (1970).
[11] Y. Syono, S. Akimoto, and K. Kohn, J. Phys. Soc. Jpn. **26**, 993 (1969).
[12] O. Chmaissem *et al.*, Phys. Rev. B **64**, 134412 (2001).
[13] G. Marasinghe, J. Han, W. James, W. Yelon, and N. Ali, J. Appl. Phys. **91**, 7863 (2002).
[14] V. Bai and T. Rajasekharan, J. Magn. Magn. Mater. **42**, 198 (1984).
[15] P. Battle, T. Gibb, and C. Jones, J. Solid State Chem. **74**, 60 (1988).
[16] A. Sacchetti, M. Baldini, F. Crispoldi, P. Postorino, P. Dore, A. Nucara, C. Martin, and A. Maignan, Phys. Rev. B **72**, 172407 (2005).
[17] H. Rietveld, J. Appl. Crystallogr. **2**, 65 (1969).
[18] J. Rodríguez-Carvajal, Physica B **192**, 55 (1993).
[19] M. I. Aroyo, J. M. Perez-Mato, C. Capillas, E. Kroumova, S. Ivantchev, G. Madariaga, A. Kirov, and H. Wondratschek, Z. Kristallogr. **221**, 15 (2006).
[20] B. L. Chamberland, A. W. Sleight, and J. F. Weiher, J. Solid State Chem. **1**, 506 (1970).
[21] *International Tables for Crystallography, Volume A: Space Group Symmetry*, edited by T. Hahn (IUCr, D. Reidel Publishing Company, Dordrecht, 1983).
[22] H. T. Stokes and D. M. Hatch, Phys. Rev. B **30**, 4962 (1984).
[23] H. T. Stokes and D. M. Hatch, *ISOTROPY*, 2002, http://stokes.byu.edu/isotropy.html
[24] E. O. Wollan *et al.*, Phys. Rev. **100**, 545 (1955).
[25] D. E. Cox, G. Shirane, R. J. Birgeneau, and J. B. MacChesney, Phys. Rev. **188**, 930 (1969).
[26] R. Sonden, P. Ravindran, S. Stolen, T. Grande, and M. Hanfland, Phys. Rev. B **74**, 144102 (2006).
[27] J. W. Allen, Phys. Rev. Lett. **36**, 1249 (1976).
[28] S. Di Matteo, N. B. Perkins, and C. R. Natoli, Phys. Rev. B **65**, 054413 (2002).
[29] C. Capillas, E. Kroumova, M. I. Aroyo, J. M. Perez-Mato, H. T. Stokes, and D. M. Hatch, J. Appl. Crystallogr. **36**, 953 (2003).